EDGE ARTICLE

Check for updates

Inter-cluster-linker-absence-enabled sub-Ångstrom pore modulation in a metal–organic framework for multi-scenario CO₂ capture†

Jia-Wen Wang, Shu-Cong Fan, Wenyu Yuan, Ying Wang [iD] and Quan-Guo Zhai [iD] *

Ultrafine aperture control of carbon capture adsorbents is first and foremost important but inscrutable. Herein, an inter-cluster-linker-absence-enabled sub-Ångstrom pore modulation strategy is proposed through the efficient transitivity of coordination bonds in a metal–organic framework (MOF). The feasibility of this strategy is well-demonstrated in SNNU-98-M materials composed of directly connected $[M_8(TAZ)_9]$ (M = Cd or Cu, TAZ = tetrazolate) triangular prism clusters. The removal of inter-cluster linkers effectively transfers the difference in coordination bond length (approximately 2.3 Å for Cd(II)−N and approximately 2.1 Å for Cu(II)−N) to the size of secondary building blocks (approximately $6.5 \times 6.5 \times 6.7$ Å³ for $[Cd_8(TAZ)_9]$ and approximately $6.2 \times 6.2 \times 6.3$ Å³ for $[Cu_8(TAZ)_9]$), and to the final MOF pore (approximately 5.5 Å for SNNU-98-Cd and approximately 5.1 Å for SNNU-98-Cu). Rational and hyperfine pore control together with optimized Lewis basic N sites endow SNNU-98-M with benchmark multi-scenario CO₂ capture performance varying from binary flue gas (CO₂/N₂) to ternary biogas (CO₂/CH₄/N₂) and even to quinary coal gas (CO₂/CH₄/N₂/CO/H₂) mixtures by a one-step process. SNNU-98-Cu is an ideal carbon capture material for practical applications due to its low-cost raw materials, easy scalablity in synthesis, ultra-high stability, and top-level selective adsorption ability as well as multi-scenario adaptability.

Introduction

With the atmospheric CO₂ concentration projected to exceed 500 ppm by 2050 due to anthropogenic emissions, the removal of greenhouse gases from dilute emissions has been identified as one of the seven chemical separations that will change the world.[1–5] Currently, CO₂ removal scenarios can be mainly divided into pre-combustion capture (biogas CO₂/CH₄/N₂ and coal gas CO₂/CH₄/N₂/CO/H₂), post-combustion capture (flue gas CO₂/N₂), and direct air capture.[6–12] The conventional amine-scrubbing method is widely used for CO₂ capture, but the absorbent regeneration consumes a large amount of energy and requires additional waste treatment processes.[13,14]

Physical adsorption is recognized as a promising carbon-capture method due to its high efficiency, easy operation, non-corrosiveness, and low energy consumption.[15–18] A large variety of adsorbents, including zeolites, porous carbon materials, and porous organic networks have been explored and applied in CO₂ removal.[19,20] From an application perspective, the construction of highly selective CO₂ adsorbents suitable for multi-scenarios such as flue gas, biogas, and coal gas is extremely necessary but remains a challenging task.[3] As a new type of adsorbent, a metal–organic framework (MOF) has the ability to rationally regulate thermodynamic and kinetic processes and is considered as an ideal platform for developing the next generation of CO₂ capture materials.[5,21] Most adsorbents are currently suitable for a single separation process,[22] and therefore, there is an urgent need to develop MOFs for multi-scenario carbon capture.

Due to the highly similar physical properties and tiny molecular size difference (usual sub-Ångstrom level, Table S1†) of the involved gas molecules, ultrafine pore regulation is important for the adsorbent design of MOFs to be used as adsorbents in multi-scenario carbon capture. However, sub-Ångstrom pore size regulation in typical MOFs containing metal clusters and inter-cluster organic linkers is not easy, although the iso-network principle and building block approach have achieved remarkable success.[23] Other common strategies including organic linker functionalization,[24–27] framework penetration,[28] and pore space partition[29] also seem powerless to solve this problem. In our opinion, the main reason for this situation is the presence of inter-cluster organic linkers. Their minor variations (*e.g.*, addition or removal of a single atom) can induce pore size fluctuations exceeding 1 Å, significantly

Key Laboratory of Applied Surface and Colloid Chemistry (MOE), Key Laboratory of Macromolecular Science of Shaanxi Province, School of Chemistry & Chemical Engineering, Shaanxi Normal University, Xi'an, Shaanxi, 710062, China. E-mail: zhaiqg@snnu.edu.cn

surpassing the sub-Ångstrom-level structural control. However, the flexibility of inter-cluster linkers may also reduce the variations in coordination bond lengths between different metal centers, resulting in nearly identical pore sizes for isostructural MOFs containing distinct metals (Scheme 1a).

Based on the above considerations, an inter-cluster-linker-absence-enabled sub-Ångstrom pore modulation strategy is proposed herein (Scheme 1b). The removal of inter-cluster linkers will generate architectures consisting of directly connected clusters,[30–32] which favorably combines the advantages of inorganic zeolites and MOFs with extra-high stability. Ultra-fine pore regulation can be achieved simply by replacing the metal nodes, which may successfully transmit the sub-Ångstrom level changes of coordination bond length to the entire pore environment.

The feasibility of this strategy is well-demonstrated in SNNU-98-M MOF materials composed of directly connected $[M_8(TAZ)_9]$ (M = Cd or Cu, TAZ = tetrazolate) triangular prism clusters. Because the ionic radius of Cu^{2+} (0.73 Å) is significantly smaller than that of Cd^{2+} (0.95 Å), the absence of inter-cluster linkers effectively transfers the difference from coordination bond length to the size of secondary building blocks and to the final MOF pore capture size (approximately 5.5 Å for SNNU-98-Cd and approximately 5.1 Å for SNNU-98-Cu). This sub-Ångstrom pore modulation is beneficial for the SNNU-98-Cu adsorbent, and enabled it to set a benchmark for challenging multi-scenario CO_2 capture ability with ultrahigh CO_2/N_2 (flue gas) selectivity (1509.3), top-level separation of ternary $CO_2/CH_4/N_2$ mixtures (biogas, breakthrough interval time of 9 min g^{-1} for N_2, 18.3 min g^{-1} for CH_4, and 80.9 min g^{-1} for CO_2), and even highly efficient one-step CO_2 capture from quinary coal gas ($CO_2/CH_4/N_2/CO/H_2$) mixtures, outperforming all advanced materials. The removal of inter-cluster linkers from SNNU-98-Cu also led to superb acid and alkali resistance stability, which lasted for 7 days in solutions with pH −0.5–13, and for as long as half a year in solutions with pH 1–12, which surpassed almost all highly stable MOF materials. In addition, rapid, efficient, and low-energy consumption reflux synthesis routes endow SNNU-98-Cu adsorbents with great potential for large-scale production and commercialization.

Results and discussion

Typical solvothermal reactions of low-cost metal salts and tetrazole ligands produce isostructural SNNU-98-M metal–organic frameworks[33,34] with a formula of $[M_5(TAZ)_9(NO_3)\cdot(H_2O)_n]$ (M = Cd^{2+}/Cu^{2+}, TAZ = tetrazolate). The production of SNNU-98-Cu can be scaled up by an ultra-fast and efficient reflux synthesis process. Only 30 min of a refluxing reaction of raw materials at 150 °C can produce 10.8 g of SNNU-98-Cu with a high yield of approximately 85% (Fig. 1, S2 and S3†). Powder X-ray diffraction (PXRD) patterns and scanning electron microscopy (SEM) images confirmed the high purity and high crystallinity of SNNU-98-Cd/Cu (Fig. S1–S3 and Table S2†) obtained by two different synthesis methods.

Single crystal structural analysis indicates that the framework of SNNU-98-Cd/Cu is formed by the direct connection of triangular prism clusters without inter-cluster organic linkers. Specifically, different metal centers result in a gap of approximately 0.2 Å in the metal–N coordination bond lengths (Cd(ɪɪ)–N of approximately 2.3 Å and Cu(ɪɪ)–N of approximately 2.1 Å) (Fig. 1a and b). Eight metals are connected through six μ_3-TAZs and three μ_4-TAZs to form $[M_8(TAZ)_9]$ clusters. The difference in metal–N bond lengths rationally resulted in a bulk reduction of the $[Cu_8(TAZ)_9]$ cluster (approximately 6.2 × 6.2 × 6.3 Å^3) compared to the $[Cd_8(TAZ)_9]$ cluster (approximately 6.5 × 6.5 × 6.7 Å^3) (Fig. 1c and d). Each $[M_8(TAZ)_9]$ cluster connects with six equal adjacent neighbors through vertex (metal) sharing patterns to generate a three-dimensional (3D) structure with typical *acs* topology.[35] Due to the removal of inter-cluster linkers, the lattice of the 3D framework formed by $[M_8(TAZ)_9]$ cluster stacking contracted due to the substitution of metallic cadmium with copper, and the c/a ratio of the cell size decreased by approximately 1% (Fig. 1e and f). Such ultrafine changes in the coordination bond length ultimately transmit to the one-dimensional hexagonal channel, which resulted in the successful achievement of sub-Ångstrom-level modulation (approximately 5.5 Å for SNNU-98-Cd and approximately 5.1 Å for SNNU-98-Cu) (Fig. 1g and h).

The permanent porosity and sub-Ångstrom pore modulation of the activated SNNU-98-Cd/Cu materials was confirmed by N_2 (77 K) and CO_2 (195 K) adsorption and desorption isotherms. As shown in Fig. 2a, SNNU-98-Cd exhibits a type I adsorption isotherm, while SNNU-98-Cu adsorbs very little N_2 at 77 K. Furthermore, CO_2 adsorption experiments at 195 K show their permanent microporosity and reversible type I adsorption isotherms (Fig. 2b), with calculated Brunauer–Emmett–Teller (BET) surface areas of 322 m^2 g^{-1} (for SNNU-98-Cd) and 212 m^2 g^{-1} (for SNNU-98-Cu). The pore size distributions of SNNU-98-Cd/Cu were calculated to be 5.1 Å and 4.8 Å, respectively, further confirming the ultra-fine pore size control, which also highly matched with their single crystal structure. Clearly, the
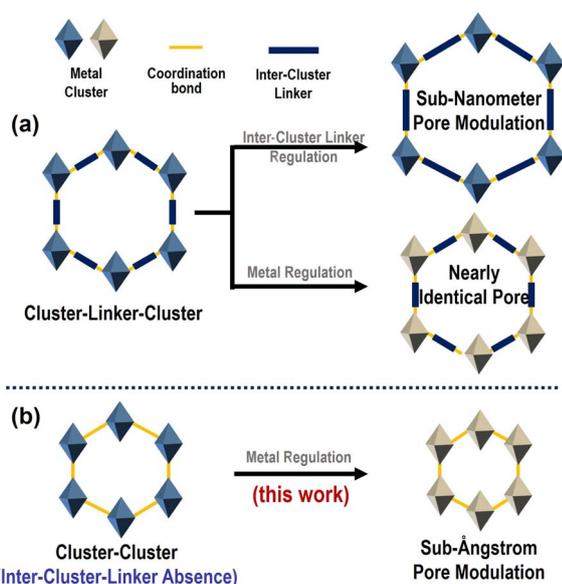
Scheme 1 The inter-cluster-linker-absence-enabled sub-Ångstrom pore modulation strategy proposed in this work.
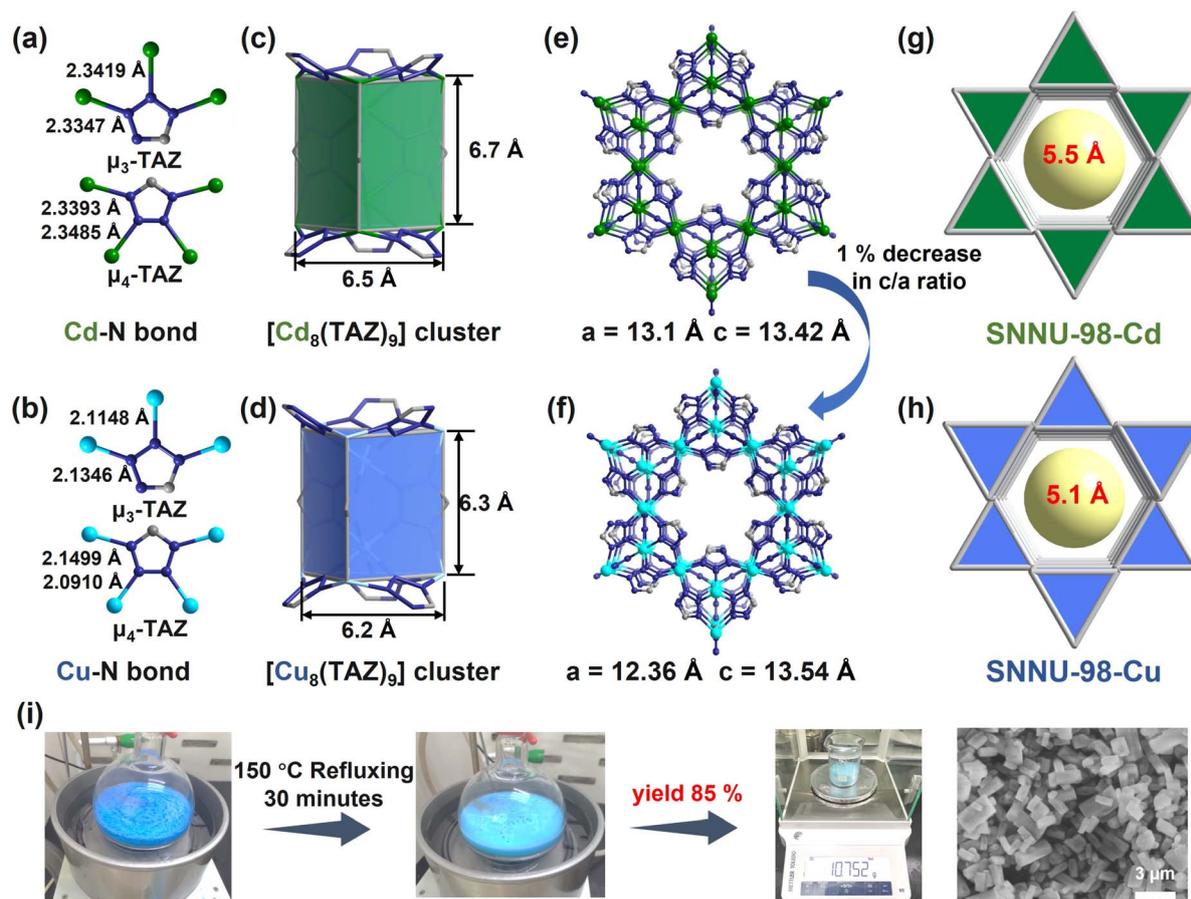
Fig. 1 Illustration of the structures and rapid reflux synthesis route of SNNU-98-Cd/Cu MOFs: (a and b) comparison of metal−N bond lengths; (c and d) detailed comparison of $[Cd_8(TAZ)_9]$ and $[Cu_8(TAZ)_9]$ clusters; (e, f, j, and h) detailed comparison of the 3D porous frameworks and 1D hexagonal channel viewed along the c-axis direction; (i) scaled-up production of SNNU-98-Cu material.

removal of inter-cluster linkers results in successful transmission of the coordination bond length gap and rational achievement of sub-Ångstrom pore regulation.

Thermal and chemical stability has long been a limitation of MOF materials for intended use in industrial applications, especially for multi-scenario CO_2 capture. These unique structural features may endow SNNU-98-Cd/Cu with ultra-high stability: (i) soft-base N sites and soft-acidic metal sites can form strong coordination bonds; (ii) tetrazolate anions with a lower pK_a value can significantly promote acid resistance; and (iii) the absence of inter-cluster linkers will increase the robustness of the MOF framework. Thermogravimetric analysis (TGA) of the synthesized and methanol-exchanged samples showed that the thermal stability is satisfactory for SNNU-98-Cd/Cu (Fig. S4†).

Furthermore, SNNU-98-Cu was immersed in pH 1–14 and 1–3 M HCl solutions to test its acid–base stability. The PXRD results showed that SNNU-98-Cu remained highly crystalline for up to 7 days in pH −0.5–13 solutions (Fig. 2c). Encouragingly, it remained stable for 6 months (pH 1–12), which is extraordinarily long and surpassed that of nearly all MOF adsorbent materials. The pH stability range and duration of SNNU-98-Cu are better than all reported Cu-MOFs, most well-known highly stable MOFs such as UiO-66,[36] ZIF-8,[37] and MOF-808,[38] and even

most of the recognized Zr-MOFs[39–41] with a high degree of connectivity (Table S3 and Fig. S5–S7†). In addition, the 195 K CO_2 adsorption of SNNU-98-Cu after the acid–base stability test showed that a high degree of crystallinity and intact pore structure was maintained (Fig. 2d and e). The adsorption capacity remained unchanged after 6 months of immersion in pH 12 solution, and the pore size distribution slightly changed, suggesting that the pore structure may have undergone a subtle collapse, but the effect on the overall gas adsorption performance was negligible. SNNU-98-Cu is capable of adapting to the complex environment of the industrial CO_2 capture process due to its low-cost raw materials, rapid scale-up reflux synthesis, and ultra-high stability.

The CO_2, CH_4, and N_2 adsorption of SNNU-98-Cd/Cu was investigated at different temperatures (Fig. S8–S13, Tables S8 and S9†) to systematically evaluate the effect of sub-Ångstrom pore regulation on selective CO_2 capture. As shown in Fig. 3a, the CO_2 adsorption by SNNU-98-Cu (124.1 cm^3 cm^{-3}) was higher than that by SNNU-98-Cd (109.1 cm^3 cm^{-3}) at 298 K and 1 bar. In addition, SNNU-98-Cu (80.1 cm^3 cm^{-3}, 64.5% at 1 bar) exhibited superior CO_2 adsorption as compared to SNNU-98-Cd (42.5 cm^3 cm^{-3}, 38.9% at 1 bar) at relatively low pressure (0.15 bar) and at 298 K, which outperformed most of the well-known MOF adsorbents, such as SIFSIX-2-Cu-i[42] (58.9 cm^3 cm^{-3}), NJU-Bai8[43] (38.1 cm^3
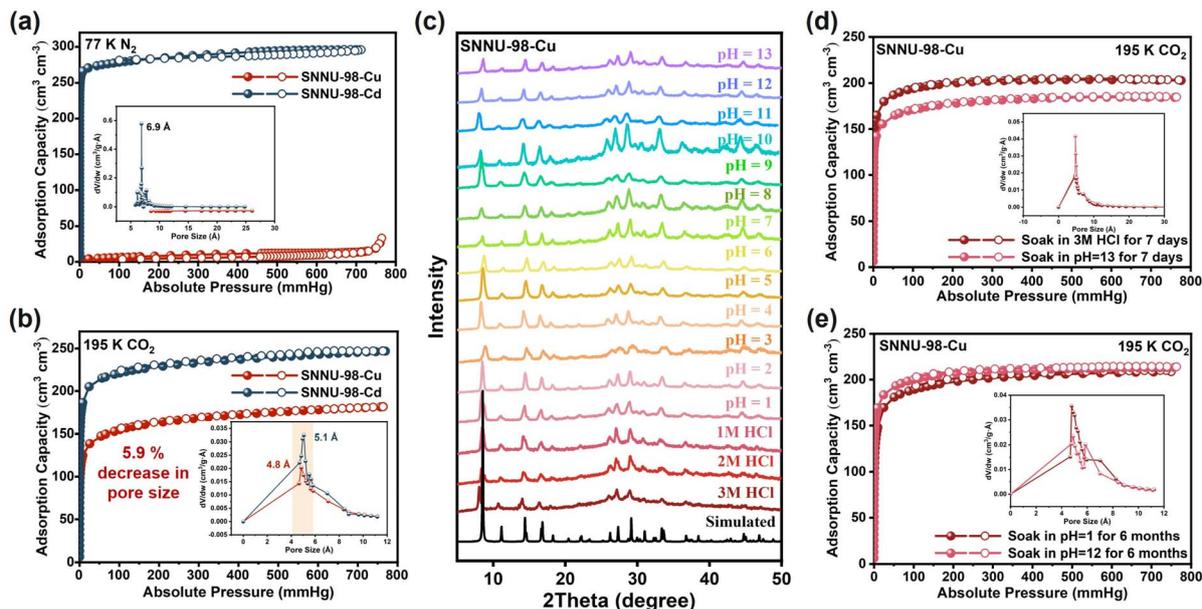
Fig. 2 Stability and porosity of SNNU-98-Cd/Cu MOFs: (a) 77 K N_2 adsorption and calculated pore size distributions; (b) 195 K CO_2 adsorption and calculated pore size distributions; (c) PXRD patterns of SNNU-98-Cu immersed in pH −0.5–13 solution for 1 week; (d and e) 195 K CO_2 adsorption curves and calculated pore size distributions of SNNU-98-Cu after immersion in −0.5–13 solution for 1 week and pH 1–12 solution for 6 months.

cm^{-3}), and Qc-5-Cu-sql[14] (24.4 cm^3 cm^{-3}) (Fig. 3b). The adjustment of the ultra-fine pore size resulted in SNNU-98-Cu with more suitable narrow pores and high-density uncoordinated tetrazolate N sites suitable for rapid mass adsorption of CO_2. Conversely, the CH_4 and N_2 uptakes on SNNU-98-Cd/Cu at 298 K and 1 bar were found to be only 37/24 cm^3 cm^{-3} and 8.4/6.2 cm^3 cm^{-3}, respectively, illustrating the molecular-sieving effect of SNNU-98-Cd/Cu. Similarly, the same adsorption characteristics were observed at 273 and 283 K (Fig. S10†).

Furthermore, the separation ratios of CO_2 *versus* CH_4 and N_2 of SNNU-98-Cu (5.2/20) were significantly higher than those of SNNU-98-Cd (2.9/13), suggesting that a sub-Ångstrom reduction in pore size favors multi-scene CO_2 separation (Fig. 3c). Notably, SNNU-98-Cd/Cu continued to maintain the original adsorption amount after multiple cycles of CO_2 adsorption and desorption, indicating good cyclic stability (Fig. 3d and S13†).

The heat of adsorption (Q_{st}) of CO_2, CH_4, and N_2 was further calculated based on the adsorption isotherms at different temperatures to understand the binding affinities between host surface and guest gas molecules (Fig. S14–S17, Tables S4 and S5†). At zero coverage, the $-Q_{st}$ values for CO_2, CH_4, and N_2 are 34.6, 20.8, and 25.9 kJ mol^{-1} for SNNU-98-Cu and 25.2, 28.6, and 35.7 kJ mol^{-1} for SNNU-98-Cd, respectively (Fig. 3g). The CO_2 adsorption affinity for SNNU-98-Cu was significantly stronger than that for SNNU-98-Cd. The affinity for CO_2 was also higher than that for CH_4 and N_2 in SNNU-98-Cu, which indicated its greater potential for CO_2 capture and separation.

Notably, the $-Q_{st}$ value for SNNU-98-Cu was at the maximum at zero loading, whereas the $-Q_{st}$ value for SNNU-98-Cd gradually increased with adsorption, which could be attributed to the smaller pore environment with stronger affinity for CO_2 at low pressure, and is consistent with the adsorption

performance. In addition, compared with other well-known CO_2 separation materials, the CO_2 adsorption enthalpy for SNNU-98-Cu is moderate, which is favorable for recycling in practical applications (Table S10†). The CO_2 temperature-programmed desorption (CO_2-TPD) curves also showed that the CO_2 desorption temperature and thermal conductivity detector (TCD) intensity for SNNU-98-Cu (123 °C) were higher than those for SNNU-98-Cd (94 °C), indicating its stronger binding with CO_2 (Fig. S18†).

The separation potentials of SNNU-98-Cd/Cu for the CO_2/N_2, CO_2/CH_4, and CH_4/N_2 mixtures were evaluated by ideal adsorbed solution theory (IAST) (Fig. S19–S27, Tables S6 and S7†). For CO_2/N_2 (15/85, v/v), the selectivity values for SNNU-98-Cd/Cu at 298 K and 1 bar were 70.1 and 1509.3, respectively (Fig. 3e). The ultra-high selectivity value for SNNU-98-Cu exceeds most of the top-level MOF adsorbents, such as ZU-301[10] (846), MUF-16[6,15] (631), NJU-Bai52[44] (581), and UTSA-16[45] (314.7). The IAST selectivity values are 8.5/94.6 for CO_2/CH_4 (50/50, v/v) and 6.5/5.3 for CH_4/N_2 (50/50, v/v), respectively, at 298 K and 1 bar (Fig. 3f and S21†). These values further indicate that SNNU-98-Cu has greater potential for separating multi-scenario CO_2 (Fig. 3h). In particular, when considering the adsorption and separation selectivity of CO_2, the comprehensive capacity of SNNU-98-Cu is superior to that of most benchmark MOF adsorbents, such as ZU-36-Ni,[4] NMMOF-9a,[3] and ZU-66[8] (Fig. 3i).

To evaluate the feasibility of the actual multi-scenario CO_2 separation process, dynamic fixed-bed breakthrough experiments were conducted for the binary gas mixtures, including flue gas (CO_2/N_2) and CO_2/CH_4, ternary biogas ($CO_2/CH_4/N_2$), and quinary coal gas ($CO_2/CH_4/N_2/CO/H_2$) (Fig. 4 and S28–S35†). For CO_2/N_2 (15/85, v/v) flue gas separation, N_2 was first observed from the column due to the lower adsorption capacity and weak
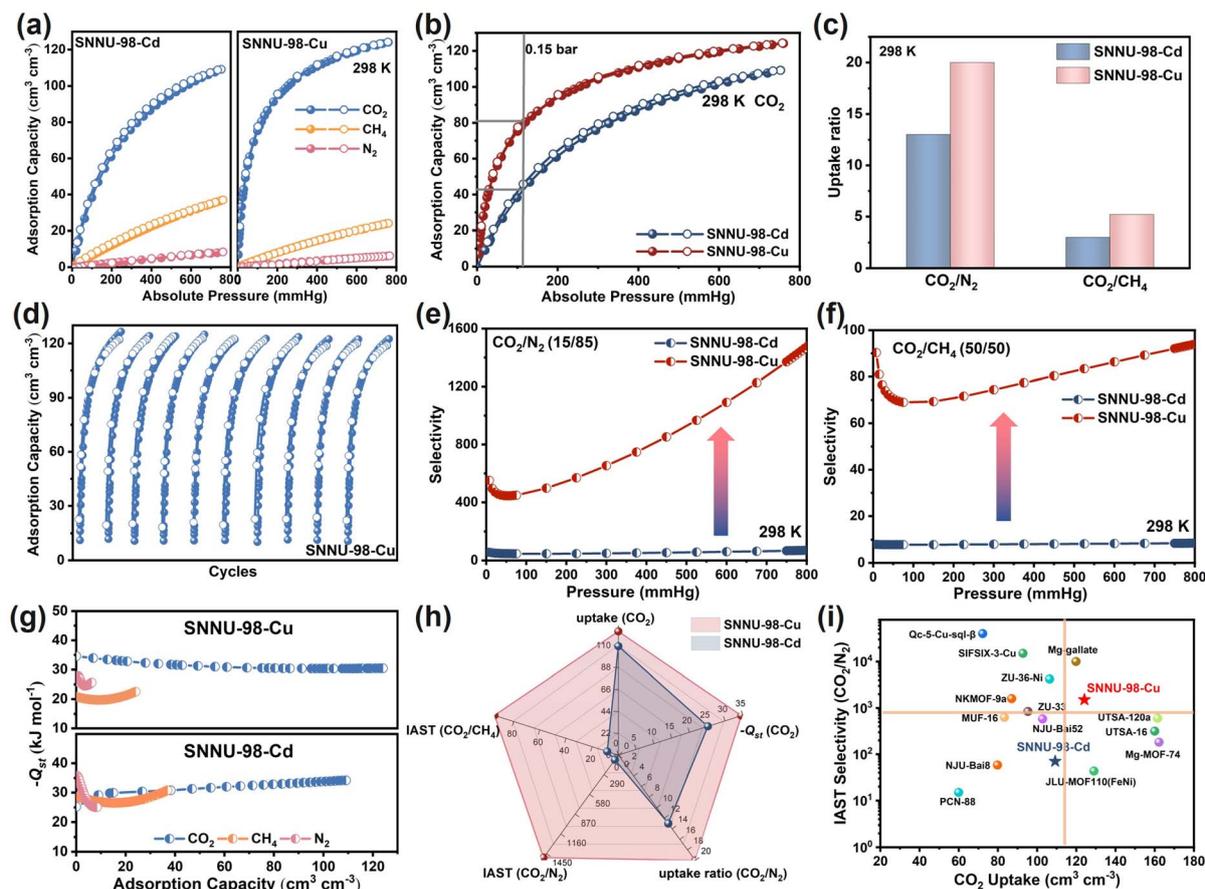
Fig. 3 Static adsorption performance of SNNU-98-Cd/Cu: (a) CO_2, CH_4, and N_2 adsorption isotherms at 298 K; (b) CO_2 adsorption isotherms at 298 K and 0.15 bar; (c) CO_2/N_2 and CO_2/CH_4 uptake ratio at 298 K; (d) CO_2 adsorption cycle stability of SNNU-98-Cu; (e and f) comparison of CO_2/N_2 and CO_2/CH_4 selectivity at 298 K; (g) heat of adsorption values for CO_2, CH_4, and N_2; (h) radar plots comparing the adsorption performance regulated by pore modulation; (i) summary of IAST selectivity (CO_2/N_2) and CO_2 uptake among reported top-level MOF adsorbents.

affinity with the MOF frameworks, whereas CO_2 was not eluted until the breakthrough interval time reached 64.4 min g^{-1} for SNNU-98-Cd and 82.6 min g^{-1} for SNNU-98-Cu, with a flow rate of 2 mL min^{-1} at 298 K (Fig. 4a). Excitingly, CO_2 was retained in the column over 109.8 min g^{-1} and 127.1 min g^{-1} at 273 K for SNNU-98-Cd and SNNU-98-Cu, respectively (Fig. S28†).

Notably, these breakthrough interval time values are superior to almost all currently used MOF adsorbents under the same conditions, such as UTSA-120a (80 min g^{-1}), JLU-MOF110 (FeNi)[2] (49.1 min g^{-1}), and ZU-66 [8] (28 min g^{-1}) and only lower than ZU-301 [10] (175 min g^{-1}) and FJI-H29 [7] (114 min g^{-1}). In addition, the interval time for SNNU-98-Cu was longer than that of SNNU-98-Cd (18.2 min g^{-1}), indicating that the sub-Ångstrom pore modulation is conducive to the separation of flue gas components. Subsequently, the separation effect of SNNU-98-Cu on the CO_2/N_2 mixed gas remained unchanged in a humid environment (50% and 98% relative humidity (RH)), indicating that it has great potential for industrial applications (Fig. S29†).

The cyclic stability of CO_2/N_2 was tested, which further demonstrated the accuracy and reproducibility of the separation performance of SNNU-98-Cu (Fig. S32†). It was noted that the breakthrough time did not proportionally decrease with increasing flow rate (Fig. 4b), which may be due to the strong

interaction between the SNNU-98-Cu adsorbent and CO_2 molecules. The high CO_2 adsorption at low pressure also indicates that the separation of CO_2/N_2 (15/85, v/v) in SNNU-98-Cu is mainly dominated by thermodynamics. The superb flue gas separation by SNNU-98-Cu was attributed to a clear thermodynamic effect, whereby CO_2 had a higher affinity for the high-density N sites of the pores in a narrower pore environment.

As for the binary biogas separation of CO_2/CH_4 (50/50, v/v), CH_4 was first observed from the column, whereas CO_2 was not eluted until the breakthrough interval time reached 29 min g^{-1} for SNNU-98-Cd and 31 min g^{-1} for SNNU-98-Cu with a flow rate of 2 mL min^{-1} at 298 K (Fig. 4c). The interval time for SNNU-98-Cu was nearly the same as that for SNNU-98-Cd, but the outflow time was much earlier (CH_4: 12, 27 min g^{-1}, CO_2: 43, 56 min g^{-1}). This may be due to the kinetic diffusion effect being greater than the thermodynamic effect for SNNU-98-Cu, resulting in the preferential outflow in SNNU-98-Cu. Furthermore, the CO_2/CH_4 separation performance was also better when compared to most of the MOF materials. When considering the materials for simultaneous separation of flue gas and biogas, SNNU-98-Cu is nearly superior to all high-performance MOFs, and second only to ZU-301 [10] (Fig. 4d and Table S11†). In addition, it also is highly advantageous for the difficult
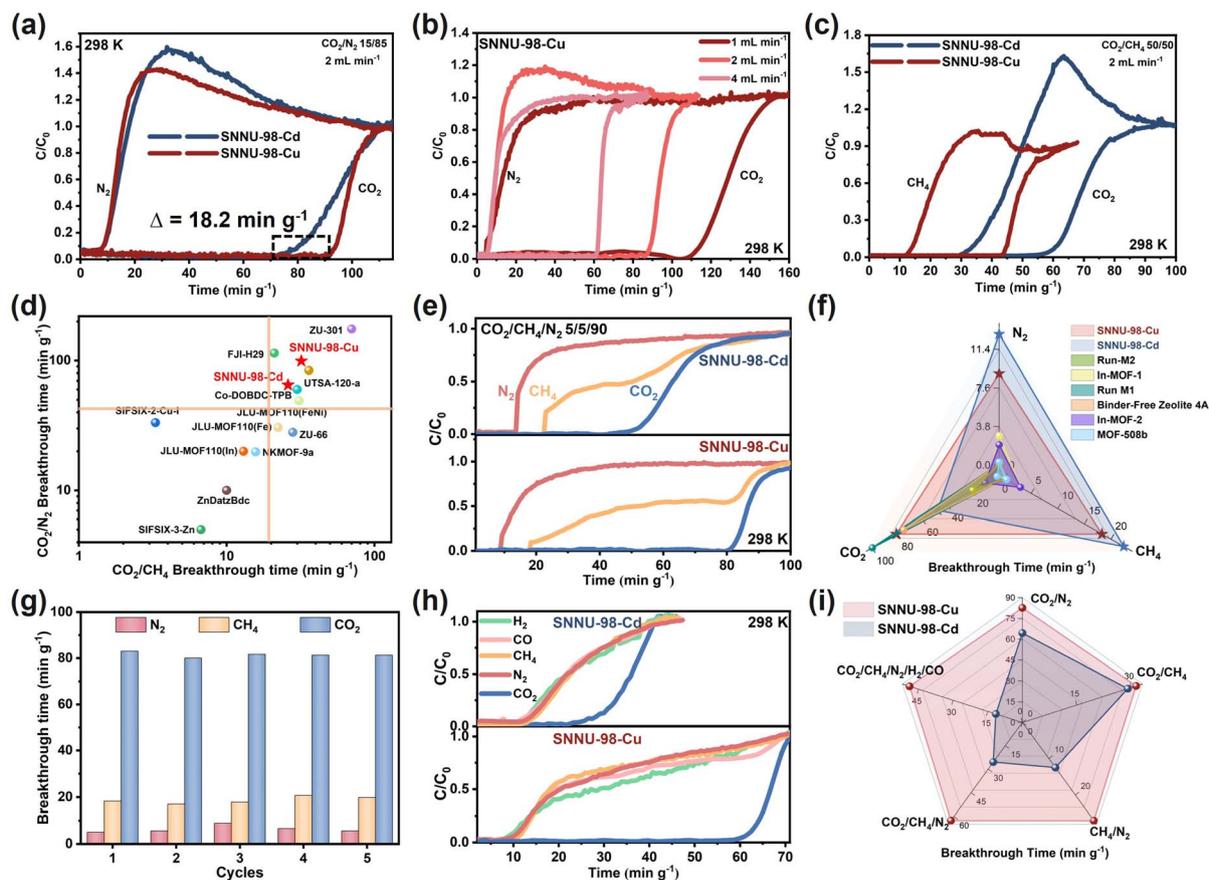
Fig. 4 The experimental breakthrough separation performance for SNNU-98-Cd/Cu: (a and c) breakthrough curves for CO_2/N_2 (15/85, v/v) and CO_2/CH_4 (50/50, v/v) gas mixtures at 298 K and 1 bar; (b) breakthrough curves for CO_2/N_2 (15/85, v/v) gas mixtures and SNNU-98-Cu at different flow rates; (d) summary of CO_2/N_2 against CO_2/CH_4 breakthrough interval times for top-level MOFs at 298 K; (e) breakthrough curves for $CO_2/CH_4/N_2$ (5/5/90, v/v/v) gas mixtures at 298 K and 1 bar; (f) comparison of $CO_2/CH_4/N_2$ three-component separation properties of the currently studied MOF materials; (g) cycling breakthrough tests for $CO_2/CH_4/N_2$ (5/5/90, v/v/v) on SNNU-98-Cu; (h) experimental breakthrough curves for $N_2/CO_2/CO/CH_4/H_2$ (66.3/14.5/9.1/5/5.1, v/v/v/v/v) gas mixtures at 298 K and 1 bar; (i) radar plots illustrating the practical separation performance regulated by the pore modulation.

problem of CH_4/N_2 (10/90, v/v) separation. N_2 was first observed from the column, whereas CH_4 was not eluted until the breakthrough interval time reached 12.5 min g^{-1} for SNNU-98-Cd and 27 min g^{-1} for SNNU-98-Cu (2 mL min^{-1} at 298 K) (Fig. S31†).

Multi-component gas separation plays an important role in adsorption separation technology, but it is still in the initial stage. We evaluated the separation of ternary biogas mixture $CO_2/CH_4/N_2$ (5/5/90, v/v/v). As shown in Fig. 4e, N_2 and CH_4 broke through the adsorption column at 12.9 and 22.4 min g^{-1}, respectively, whereas CO_2 was not detected at the exit until 47.9 min g^{-1} for SNNU-98-Cd. Notably, the shrinking of pore size produced a much better performance, with the outflow of N_2 detected at 9 min g^{-1}, while the outflow of CH_4 and CO_2 from the column was 18.3 and 80.9 min g^{-1}, respectively. Such separation of the $CO_2/CH_4/N_2$ ternary gas mixture in a single process is unprecedented. The separation ability was further promoted as the temperature decreased, and was superior to all adsorbent materials that were used in this separation process (Fig. 4f and Table S12†). Notably, the CH_4 breakthrough curve shows a plateau region in the middle stage, which is due to the presence of competing adsorption. Simultaneous adsorption

and desorption of CH_4 occurs until CO_2 adsorption is saturated, and then, the C/C_0 rises to 1. In addition, the cyclic stability of this three-component separation is excellent (Fig. 4g). Subsequently, real industrial separation ratios ($CO_2/CH_4/N_2$: 30/65/5 and 40/55/5, v/v/v) for SNNU-98-Cu were further simulated, which showed that N_2 broke through at 6 min g^{-1}, and CH_4 at 23 and 29 min g^{-1}, respectively, while CO_2 was not detected until 88 and 80 min g^{-1}. This further confirmed that SNNU-98-Cu has great potential for industrial applications (Fig. S34†).

Furthermore, the adsorption capacities were calculated from the breakthrough curves and compared with single-component gas adsorption (Tables S13 and S14†). The results showed that the low-pressure CO_2 breakthrough capacity of SNNU-98-Cu was higher than that of SNNU-98-Cd. For CO_2/N_2 (15/85, v/v) at 298 K, the CO_2 adsorption capacity of SNNU-98-Cu/Cd was calculated to be 56.9 and 64.6 cm^3 cm^{-3} compared to 41.2 and 80 cm^3 cm^{-3} for static adsorption, respectively. This is also consistent with GCMC simulation and $-Q_{st}$ values, which further confirms that the separation effect conferred by SNNU-98-Cu is satisfactory.

To further demonstrate the multi-scenario adaptability of SNNU-98-Cd/Cu adsorbents, low calorific value coal gas with a practical composition of $N_2/CO_2/CO/H_2O/CH_4/H_2$ (58.4/14.5/9.1/8/5.1/4.8, v/v/v/v/v/v) was selected. Extraordinarily, SNNU-98-Cd/Cu can realize efficient one-step CO_2 capture from this five-component gas mixture (Fig. 4h). The N_2, CO, CH_4, and H_2 gas components concurrently broke through the adsorption column at 10 min g^{-1}, whereas CO_2 was not detected exiting until 21.5 and 58.9 min g^{-1} for SNNU-98-Cd and SNNU-98-Cu, respectively. Notably, SNNU-98-Cd/Cu also possessed a high water vapor adsorption capacity (Fig. S36†), which further indicated that these robust MOFs without inter-cluster linkers are suitable for complex industrial separation scenarios and will achieve unprecedented separation results.

Overall, SNNU-98-Cu benefits from an inter-cluster-linker-absence-enabled sub-Ångstrom pore modulation, and its comprehensive CO_2 capture ability is much more optimal than that of SNNU-98-Cd (Fig. 4i). The ultra-microporous environments coupled with the high density of bare tetrazolate N sites leads to the strongest interactions with CO_2 molecules and achieved efficient multi-scenario separation with thermodynamic and kinetic synergy.

In situ infrared (IR) spectroscopic measurements further probed the interaction of SNNU-Cd/Cu with CO_2 and CH_4, whereas the N_2 molecule has a high degree of symmetry and absorbs IR light very weakly (Fig. 5 and S37–S38†). The results show that the CO_2 asymmetric telescopic vibrational peaks ($v_3 = 2349$ cm^{-1}) are redshifted, and the bending vibrational peaks ($v_2 = 667$ cm^{-1}) are split, which proves that CO_2 strongly interacts with SNNU-98-Cd/Cu. As shown in Fig. 5a and b, CO_2-loaded SNNU-98-Cu (2335–2316 cm^{-1}) is redshifted more than SNNU-98-Cd (2338–2327 cm^{-1}).

The positional differences of SNNU-98-Cd/Cu bending vibrational peak splitting were 8 cm^{-1} and 30 cm^{-1}, respectively, and the vibrational peaks of SNNU-98-Cu at 3000–3250 cm^{-1} were significantly stronger than those of SNNU-98-Cd, indicating a stronger C–H⋯O$_{CO_2}$ interaction between SNNU-98-Cu and CO_2. With the increase in pressure, the characteristic peak of CH_4-loaded SNNU-98-Cd/Cu appeared at 3015 cm^{-1}, and it gradually enhanced (Fig. 5c and d). The spectra of CO_2 and CH_4 at low pressure indicated that the peaks of SNNU-98-Cu are stronger than those of SNNU-98-Cd, which further proved that the affinity of SNNU-98-Cu for CO_2 and CH_4 was very strong (Fig. 5e and f). All these results not only validate the above adsorption separation performance but also illustrate the power of sub-Ångstrom pore modulation on multi-scenario CO_2 capture.

To gain further insight into the host–guest interactions and adsorption behavior at the molecular level, grand canonical Monte Carlo (GCMC) simulations were performed. As shown in Fig. 6, SNNU-98-Cd and SNNU-98-Cu obviously adsorb different amounts of gas molecules in a certain channel, at 298 K and 1 bar. SNNU-98-Cu adsorbed significantly more CO_2 molecules than SNNU-98-Cd, and the amount of CO_2 exceeded that of CH_4 and N_2, indicating that the interaction of CO_2 was stronger in smaller pores. This is very useful for efficient capture of CO_2 from multiple industrial scenarios.

As shown in Fig. S39,† the binding sites of CO_2 mainly interact with high-density bare tetrazolate N sites and hydrogen bond with H, where the interaction with SNNU-98-Cu (N⋯C$_{CO_2}$: 2.7861–3.6808 Å, C–H⋯O$_{CO_2}$: 2.3646–3.108 Å) is significantly stronger than that with SNNU-98-Cd (N⋯C$_{CO_2}$: 3.6063–3.9138 Å, C–H⋯O$_{CO_2}$: 2.8270–3.4154 Å), and thus, it can adsorb additional CO_2 molecules. It was confirmed that the reduced pore size at the Ångstrom level enhances the interaction between the framework and CO_2. However, CH_4 molecules with larger kinetic diameters undergo weaker N⋯H–C$_{CH_4}$ interactions with N atoms in the pores (2.9424–3.8830 Å for SNNU-98-Cd, and 2.5317–3.0746 Å for SNNU-98-Cu). This indicates that CH_4 diffuses more slowly in the micropores, and SNNU-98 can

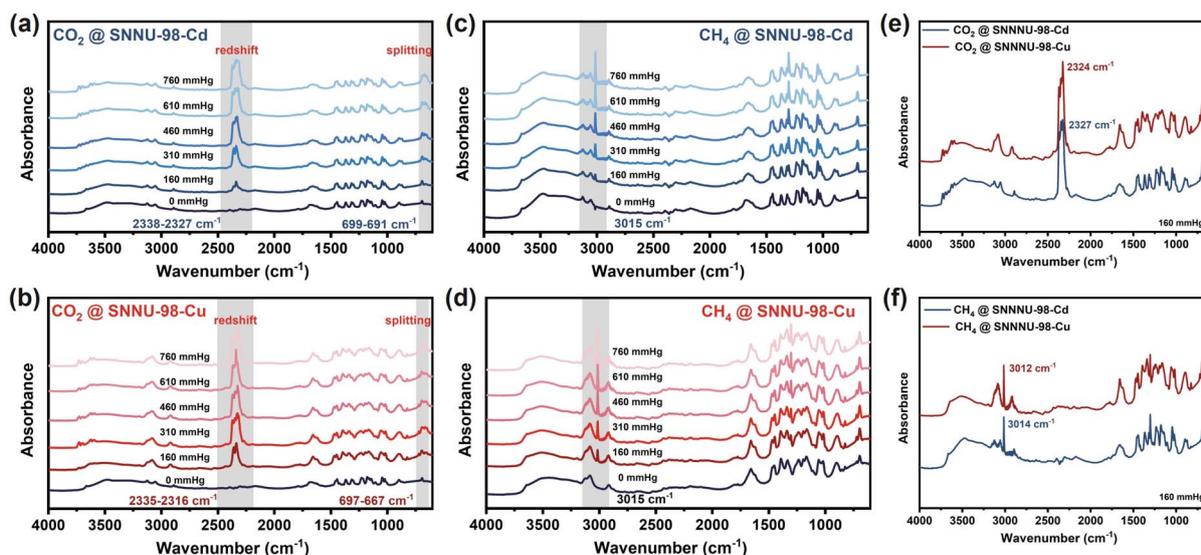**Fig. 5** *In situ* FT-IR spectra for SNNU-98-Cd/Cu: (a and b) for the CO_2 adsorption process; (c and d) for the CH_4 adsorption process; (e and f) comparison of CO_2 and CH_4 adsorption.
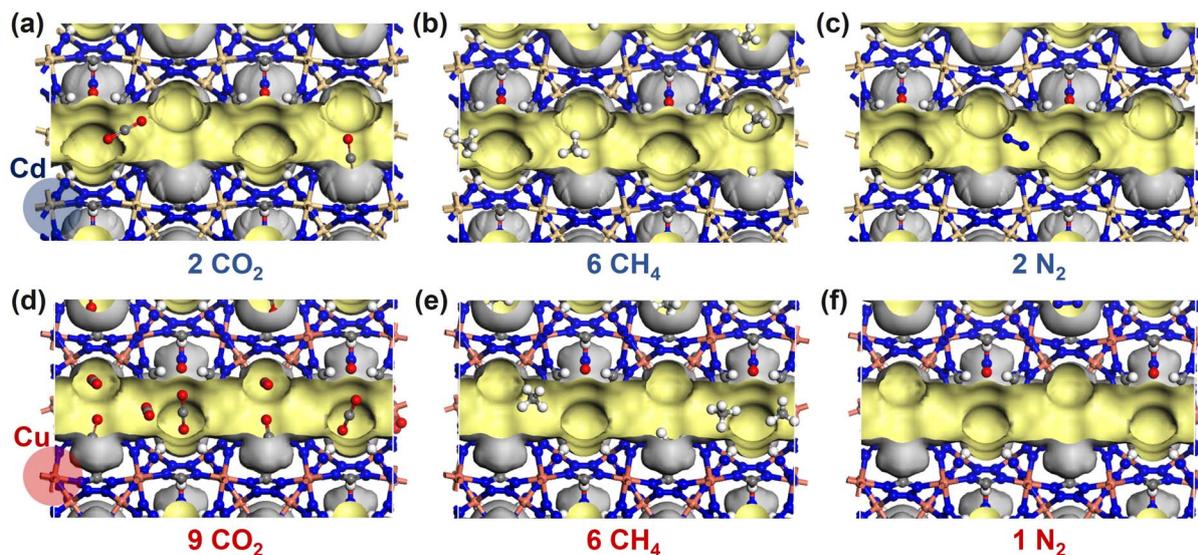
Fig. 6 GCMC-simulated (a and d) CO_2, (b and e) CH_4, and (c and f) N_2 distributions in the channel of SNNU-98-Cd/Cu MOFs.

efficiently separate CO_2 and CH_4 by kinetic sieving. In addition, the polarizability and quadrupole moment of N_2 are lower than those of CO_2, and thus, the interaction with SNNU-98-Cu ($H \cdots N_{N_2}$: 2.8799–3.8322 Å) and SNNU-98-Cd ($H \cdots N_{N_2}$: 2.5857–3.9138 Å) is weaker, suggesting an excellent separation of CO_2 and N_2 based on thermodynamic principles. Subsequently, the density distributions of different gas molecules were further calculated, which clearly showed that the interaction between CO_2 and the SNNU-98-Cd/Cu adsorbents was stronger than those of CH_4 and N_2. The CO_2 distribution density in SNNU-98-Cu was significantly higher than that of SNNU-98-Cd, especially in the low-pressure region (Fig. S40–S44†). This further demonstrates that the interaction of CO_2 in smaller pores is stronger, thereby benchmarking the capture of CO_2 in multiple scenarios (flue gas, biogas, and coal gas).

Conclusions

In this work, we propose a rational sub-Ångstrom pore modulation strategy for metal–organic frameworks by the removal of inter-cluster linkers. With the absence of inter-cluster linkers, tiny changes in coordination bond lengths triggered by metal regulation can be efficiently transmitted, enabling ultra-fine pore size control and further significantly promoting multi-scenario CO_2 capture performance. Due to the suitable pore environment and high density of bare N sites, SNNU-98-Cu exhibits ultra-high stability (pH -0.5–13), top-level CO_2/N_2 selectivity (1509.3), and CO_2 capture ability superior to nearly all porous adsorbent material, which can efficiently separate CO_2 from binary flue gas, ternary biogas, and quinary coal gas mixtures in one step. *In situ* IR spectra and GCMC calculations clearly indicate that the benchmark CO_2 capture performance is due to the coupling effect of thermodynamics and dynamics in the ultra-micropore space. This work introduces a valid strategy realizing hyperfine pore size regulation of MOF adsorbent and prompts the CO_2 capture from 'single-scene passive adaptation' to 'multi-scene active response', which may provide the combination of high efficiency, economy, and sustainability for industrial carbon emission reduction.

Data availability

All the associated data are available in the ESI.†

Author contributions

Q.-G. Z. and J.-W. W. conceived the idea for this research. J.-W. W. carried out the experiments, analyzed the results, and wrote the manuscript. Q.-G. Z. led the project and edited the manuscript. All authors participated in and contributed to the preparation of the manuscript.

Conflicts of interest

There are no conflicts to declare.

Acknowledgements

Notes and references

1 L. Zhang, Z. He, Y. Liu, J. You, L. Lin, J. Jia, S. Chen, N. Hua, L.-A. Ma, X. Ye, Y. Liu, C.-X. Chen and Q. Wang, *ACS Appl. Mater. Interfaces*, 2023, **15**, 30394–30401.
2 W. Li, X. Liu, X. Yu, B. Zhang, C. Ji, Z. Shi, L. Zhang and Y. Liu, *Inorg. Chem.*, 2023, **62**, 18248–18256.
3 S. Geng, H. Xu, C.-S. Cao, T. Pham, B. Zhao and Z. Zhang, *Angew. Chem., Int. Ed.*, 2023, **62**, e202305390.

4 Z. Zhang, Q. Ding, S. B. Peh, D. Zhao, J. Cui, X. Cui and H. Xing, *Chem. Commun.*, 2020, **56**, 7726–7729.

5 F. Chen, J. Wang, L. Guo, X. Huang, Z. Zhang, Q. Yang, Y. Yang, Q. Ren and Z. Bao, *Sep. Purif. Technol.*, 2022, **292**, 121031.

6 O. T. Qazvini and S. G. Telfer, *ACS Appl. Mater. Interfaces*, 2021, **13**, 12141–12148.

7 D. Wu, C. Liu, J. Tian, F. Jiang, D. Yuan, Q. Chen and M. Hong, *Inorg. Chem.*, 2020, **59**, 13542–13550.

8 L. Yang, X. Cui, Y. Zhang, Q. Wang, Z. Zhang, X. Suo and H. Xing, *ACS Sustain. Chem. Eng.*, 2019, **7**, 3138–3144.

9 A. Pal, S. Chand, S. M. Elahi and M. C. Das, *Dalton Trans.*, 2017, **46**, 15280–15286.

10 C. Yu, Q. Ding, J. Hu, Q. Wang, X. Cui and H. Xing, *Chem. Eng. J.*, 2021, **405**, 126937.

11 J.-R. Li, J. Yu, W. Lu, L.-B. Sun, J. Sculley, P. B. Balbuena and H.-C. Zhou, *Nat. Commun.*, 2013, **4**, 1538.

12 Z. Zhou, T. Ma, H. Zhang, S. Chheda, H. Li, K. Wang, S. Ehrling, R. Giovine, C. Li, A. H. Alawadhi, M. M. Abduljawad, M. O. Alawad, L. Gagliardi, J. Sauer and O. M. Yaghi, *Nature*, 2024, **635**, 96–101.

13 O. Shekhah, Y. Belmabkhout, Z. Chen, V. Guillerm, A. Cairns, K. Adil and M. Eddaoudi, *Nat. Commun.*, 2014, **5**, 4228.

14 K.-J. Chen, D. G. Madden, T. Pham, K. A. Forrest, A. Kumar, Q.-Y. Yang, W. Xue, B. Space, J. J. Perry, J.-P. Zhang, X.-M. Chen and M. J. Zaworotko, *Angew. Chem., Int. Ed.*, 2016, **55**, 10268–10272.

15 O. T. Qazvini, R. Babarao and S. G. Telfer, *Nat. Commun.*, 2021, **12**, 197.

16 Q. Shi, *J. Fuel Chem. Technol.*, 2021, **49**, 1531–1539.

17 D. Song, S. Zou, Z. Ji, Y. Li, H. Li, Y. Zhou, C. Chen, Q. Chen and M. Wu, *Angew. Chem., Int. Ed.*, 2025, **64**, e202423496.

18 Z. Wang, Y. Zhang, E. Lin, S. Geng, M. Wang, J. Liu, Y. Chen, P. Cheng and Z. Zhang, *J. Am. Chem. Soc.*, 2023, **145**, 21483–21490.

19 L. F. A. S. Zafanelli, A. Henrique, M. Karimi, A. E. Rodrigues and J. A. C. Silva, *Ind. Eng. Chem. Res.*, 2020, **59**, 13724–13734.

20 B. Li, S. Wang, Z. Tian, G. Yao, H. Li and L. Chen, *Adv. Theory Simul.*, 2022, **5**, 2100378.

21 E. Aly, L. F. A. S. Zafanelli, A. Henrique, M. Golini Pires, A. E. Rodrigues, K. Gleichmann and J. A. C. Silva, *Ind. Eng. Chem. Res.*, 2021, **60**, 15236–15247.

22 E. Wu, X.-W. Gu, D. Liu, X. Zhang, H. Wu, W. Zhou, G. Qian and B. Li, *Nat. Commun.*, 2023, **14**, 6146.

23 X. Feng, X. Wang, H. Yan, H. Liu, X. Liu, J. Guan, Y. Lu, W. Fan, Q. Yue and D. Sun, *Angew. Chem., Int. Ed.*, 2024, **63**, e202407240.

24 J. Wang, Y. Zhang, Y. Su, X. Liu, P. Zhang, R.-B. Lin, S. Chen, Q. Deng, Z. Zeng, S. Deng and B. Chen, *Nat. Commun.*, 2022, **13**, 200.

25 S. Yuan, L. Huang, Z. Huang, D. Sun, J.-S. Qin, L. Feng, J. Li, X. Zou, T. Cagin and H.-C. Zhou, *J. Am. Chem. Soc.*, 2020, **142**, 4732–4738.

26 W. Fan, X. Zhang, Z. Kang, X. Liu and D. Sun, *Coord. Chem. Rev.*, 2021, **440**, 213968.

27 S. Yuan, Y.-P. Chen, J.-S. Qin, W. Lu, L. Zou, Q. Zhang, X. Wang, X. Sun and H.-C. Zhou, *J. Am. Chem. Soc.*, 2016, **138**, 8912–8919.

28 H.-L. Jiang, T. A. Makal and H.-C. Zhou, *Coord. Chem. Rev.*, 2013, **257**, 2232–2249.

29 Y. Ye, Z. Ma, R.-B. Lin, R. Krishna, W. Zhou, Q. Lin, Z. Zhang, S. Xiang and B. Chen, *J. Am. Chem. Soc.*, 2019, **141**, 4130–4136.

30 J.-W. Wang, S.-C. Fan, Z. Li, Q.-Q. Zhang, Y.-F. Zhang, Z.-Y. Wang, W. Yuan, Y. Wang and Q.-G. Zhai, *Adv. Funct. Mater.*, 2024, **35**, 2420070.

31 S. P. Chan and Y. Zhang, *Chem. - Eur. J.*, 2023, **29**, e202301279.

32 Q.-G. Zhai, C.-Z. Lu, S.-M. Chen, X.-J. Xu and W.-B. Yang, *Cryst. Growth Des.*, 2006, **6**, 1393–1398.

33 Z.-J. Hou, Z.-Y. Liu, N. Liu, E.-C. Yang and X.-J. Zhao, *Dalton Trans.*, 2015, **44**, 2223–2233.

34 J.-W. Wang, S.-C. Fan, H.-P. Li, X. Bu, Y.-Y. Xue and Q.-G. Zhai, *Angew. Chem., Int. Ed.*, 2023, **62**, e202217839.

35 Z. Chen, P. Li, R. Anderson, X. Wang, X. Zhang, L. Robison, L. R. Redfern, S. Moribe, T. Islamoglu, D. A. Gómez-Gualdrón, T. Yildirim, J. F. Stoddart and O. K. Farha, *Science*, 2020, **368**, 297–303.

36 M. Kandiah, M. H. Nilsen, S. Usseglio, S. Jakobsen, U. Olsbye, M. Tilset, C. Larabi, E. A. Quadrelli, F. Bonino and K. P. Lillerud, *Chem. Mater.*, 2010, **22**, 6632–6640.

37 K. Leus, T. Bogaerts, J. De Decker, H. Depauw, K. Hendrickx, H. Vrielinck, V. Van Speybroeck and P. Van Der Voort, *Microporous Mesoporous Mater.*, 2016, **226**, 110–116.

38 W. Liang, H. Chevreau, F. Ragon, P. D. Southon, V. K. Peterson and D. M. D'Alessandro, *CrystEngComm*, 2014, **16**, 6530–6533.

39 H. Yang, F. Peng, A. N. Hong, Y. Wang, X. Bu and P. Feng, *J. Am. Chem. Soc.*, 2021, **143**, 14470–14474.

40 H.-L. Jiang, D. Feng, K. Wang, Z.-Y. Gu, Z. Wei, Y.-P. Chen and H.-C. Zhou, *J. Am. Chem. Soc.*, 2013, **135**, 13934–13938.

41 Y. Duan, H. Li, X. Shi, C. Ji, J. Imbrogno and D. Zhao, *Ind. Eng. Chem. Res.*, 2025, **64**, 5372–5382.

42 P. Nugent, Y. Belmabkhout, S. D. Burd, A. J. Cairns, R. Luebke, K. Forrest, T. Pham, S. Ma, B. Space, L. Wojtas, M. Eddaoudi and M. J. Zaworotko, *Nature*, 2013, **495**, 80–84.

43 L. Du, Z. Lu, K. Zheng, J. Wang, X. Zheng, Y. Pan, X. You and J. Bai, *J. Am. Chem. Soc.*, 2013, **135**, 562–565.

44 X. Song, M. Zhang, C. Chen, J. Duan, W. Zhang, Y. Pan and J. Bai, *J. Am. Chem. Soc.*, 2019, **141**, 14539–14543.

45 S. Xiang, Y. He, Z. Zhang, H. Wu, W. Zhou, R. Krishna and B. Chen, *Nat. Commun.*, 2012, **3**, 954.